ANTIOXIDANTS & REDOX SIGNALING
Volume 00, Number 00, 2015
© Mary Ann Liebert, Inc.
DOI: 10.1089/ars.2015.6390

FORUM REVIEW ARTICLE

Quantitative Redox Imaging Software

Mark D. Fricker

Abstract

Significance: A wealth of fluorescent reporters and imaging systems are now available to characterize dynamic physiological processes in living cells with high spatiotemporal resolution. The most reliable probes for quantitative measurements show shifts in their excitation or emission spectrum, rather than just a change in intensity, as spectral shifts are independent of optical path length, illumination intensity, probe concentration, and photobleaching, and they can be easily determined by ratiometric measurements at two wavelengths. ***Recent Advances:*** A number of ratiometric fluorescent reporters, such as reduction-oxidation-sensitive green fluorescent protein (roGFP), have been developed that respond to the glutathione redox potential and allow redox imaging *in vivo*. roGFP and its derivatives can be expressed in the cytoplasm or targeted to different organelles, giving fine control of measurements from sub-cellular compartments. Furthermore, roGFP can be imaged with probes for other physiological parameters, such as reactive oxygen species or mitochondrial membrane potential, to give multi-channel, multi-dimensional 4D (*x,y,z,t*) images. ***Critical Issues:*** Live cell imaging approaches are needed to capture transient or highly spatially localized physiological behavior from intact, living specimens, which are often not accessible by other biochemical or genetic means. ***Future Directions:*** The next challenge is to be able to extract useful data rapidly from such large (GByte) images with due care given to the assumptions used during image processing. This article describes a suite of software programs, available for download, that provide intuitive user interfaces to conduct multi-channel ratio imaging, or alternative analysis methods such as pixel-population statistics or image segmentation and object-based ratio analysis. *Antioxid. Redox Signal.* 00, 000–000.

Introduction

RATIOMETRIC METHODS for quantitative imaging of physiological parameters using fluorescent reporters in living cells were developed in the 1980s to compensate for varying optical path length, illumination intensity, probe concentration, and photobleaching (2, 21). Since then, the ratiometric approach has been adapted to confocal, multi-photon, and super-resolution systems, and has inspired the development of numerous ratioable fluorescent probes, including genetically encoded fluorescent proteins, that either show intrinsic spectral shifts on binding the ion or ligand of interest or are linked to form bi-molecular FRET (Förster resonance energy transfer) sensors (1, 10, 11, 22). The key elements for quantitative ratio imaging are a fluorescent probe that shows a shift in excitation or emission spectrum with changes in the parameter of interest, and an imaging system that is capable of rapidly switching between excitation wavelengths for dual-excitation probes, or simultaneous measurement at two emission wavelengths for dual-emission probes.

While imaging animal cells in culture is optically straightforward, plants and fungi pose additional challenges for reliable measurements, as (1) the cells of interest do not grow on the coverslip, but exist in large, optically complex tissues with refractile components and absorbing elements; (2) cells are large, but the cytoplasm is only present as a thin layer between the vacuole and cell wall or in trans-vacuolar stands that require 3D (*x,y,z*) sampling to be captured effectively; (3) the cytoplasm and organelles move rapidly, necessitating fast temporal sampling; and (4) there are high levels of auto-fluorescence that require additional bleed-through correction and masking. It is also increasingly important to correlate the parameter of interest, such as redox potential, with morphological or developmental changes in the specimen, or with other physiological parameters, such as

Department of Plant Sciences, University of Oxford, Oxford, United Kingdom.

reactive oxygen species (ROS), imaged simultaneously with additional fluorescent probes in multi-channel measurements.

The challenge is then to develop convenient software packages that are capable of extracting useful information from such large (GByte), multi-dimensional images (see for example, FluoQ for ImageJ, 19). In response to this need, the programs described here were written to visualize and analyze ratiometric changes in fluorescence of the dual-excitation redox-sensitive protein, reduction-oxidation-sensitive green fluorescent protein (roGFP) and its derivatives, expressed in transgenic cell cultures, plants, and fungi, alongside other physiological parameters, such as ROS or mitochondrial activity, in multi-dimensional 4D (*x,y,z,t*) images. While developed for redox imaging, in practice, the programs can also be used to quantify fluorescent signals from any ratiometric (or single-wavelength) probe in any system.

Ratio Analysis Software Overview

An overview of the functionality of the software suite is shown in Figure 1. There are separate interfaces to import and preprocess images before ratio analysis (Fig. 1A, B: import module), conduct a basic ratio analysis (Fig. 1C, D: basic ratio analysis module), and include additional fluorescence channels to allow correlation between multiple physiological parameters (Fig. 1E, F: advanced ratio analysis module), which also allows pixel-population measurements to handle complex structures that are not readily sampled by manual measurements from discrete regions of interest (ROI); and object-based segmentation approaches, coupled with morphological characterization to correlate organelle physiology with spatial landmarks (Fig. 1G, H: object-based ratio analysis module). The programs are written in MatLab (The Mathworks) and packaged in a single compiled executable file, or available as the original matlab files, for download from www.markfricker.org. A complete manual is also provided in the download package.

Image import and preprocessing

The programs use a common import module (Fig. 1A, B) to load images from a variety of formats. Each program progresses through the ratio analysis step by step, to ensure that due consideration is explicitly given to each of the parameters used in the analysis. Once set, the processing and calibration parameters can be stored in a database and reapplied to subsequent analyses or datasets.

The starting point for analysis is a multi-channel, multidimensional fluorescence image (Fig. 1A), often with a corresponding (non-confocal) bright-field image (Fig. 1B). Visualization of the probe response involves calculation of pseudo-color-coded ratio images that help the user understand the spatiotemporal dynamics in different cells or subcellular compartments. Ratio images are calculated on a pixel-by-pixel basis from images collected at wavelengths that preferentially excite the oxidized and reduced form of the probe. For roGFP on current laser-based confocal microscopes, these are typically 405 and 488 nm, respectively.

Pixel-by-pixel ratioing is critically dependent on correct image registration, as even very slight misalignment of the ratio images yields obvious fringing with completely inappropriate ratios along the boundaries. During data collection using confocal systems, this typically means that line switching, rather than frame switching between excitation wavelengths must be used to minimize the impact of organelle or specimen movement. During data processing, it is possible to correct for minor channel misalignment by calculating the (sub)-pixel offsets that maximize the cross-correlation between the selected image(s) and a reference image, typically the channel with the brightest and best resolved features. Images are then aligned using bi-linear interpolation with these offsets [Fig. 1A (i)].

Likewise, time-series measurements of intact specimens in perfusion systems often experience some level of drift in the (*x,y*) plane or focus shift along the *z*-axis. It is helpful to align the image series to ensure measurements are made from the same region of the specimen in subsequent analysis. Specimen movement or stage drift can be partially compensated by (*x,y*) registration using temporal cross-correlation [Fig. 1A (ii)].

While many animal cells conveniently grow as a monolayer on a coverslip greatly facilitating imaging with a single optical section or using total internal reflection fluorescence (TIRF) microscopy, a number of optical sections are often required to capture features of interest in plant and fungal cells. When visualizing morphological markers, such as organelle markers, 3D (*x,y,z*) data are often visualized as a maximum intensity projection (MIP) along the *z*-axis for each channel. However, this is not appropriate as a precursor to quantitative measurements, particularly when ratioing two channels, as the MIP selects the ''noisiest'' pixel at the extreme of the intensity distribution along the *z*-axis, and will pick out pixels from different positions in *z* for each channel, making it impossible to calculate a reliable ratio image.

An average brightness projection in *z* provides better noise reduction, and it may be useful for simple objects that do not overlap in the *z*-axis. However, a more appropriate approach is to apply local noise reduction by smoothing in (*x,y,z*), select the *z*-position of the brightest voxel in one, or a sub-set of channels, and extract the same (*x,y,z*) voxel from all the other channels [Fig. 1A (iii)]. This provides a sub-sample of the original 3D data that faithfully preserves the main features of interest in the *z*-axis, and is absolutely required if different channels are going to be ratioed later on to ensure that information from the same (averaged) voxels are compared. This approach also compensates to some extent for axial movement, as the brightest object is extracted irrespective of its *z*-position.

Basic ratio analysis

The basic ratio analysis program (Fig. 1C, D) is designed to analyze single (*x,y*) images, 3D (*x,y,t*) time series, or 3D (*x,y,z*) *z*-stacks. The first processing step usually involves improving the signal-to-noise ratio (S/N) by spatial or temporal averaging [Fig. 1D (i)]. While there are a range of noise-reduction algorithms available, simple averaging using 2D or 3D kernels of different sizes provides a balance between S/N and spatiotemporal resolution. Averaging can be usefully combined with sub-sampling to reduce image sizes and increase processing speed, as spatial resolution is already compromised by averaging. As averaging is likely to yield noninteger values, this step also requires conversion from integer to floating-point format.

To measure intensity values correctly, it is important that the images are collected with a nonzero background, so that

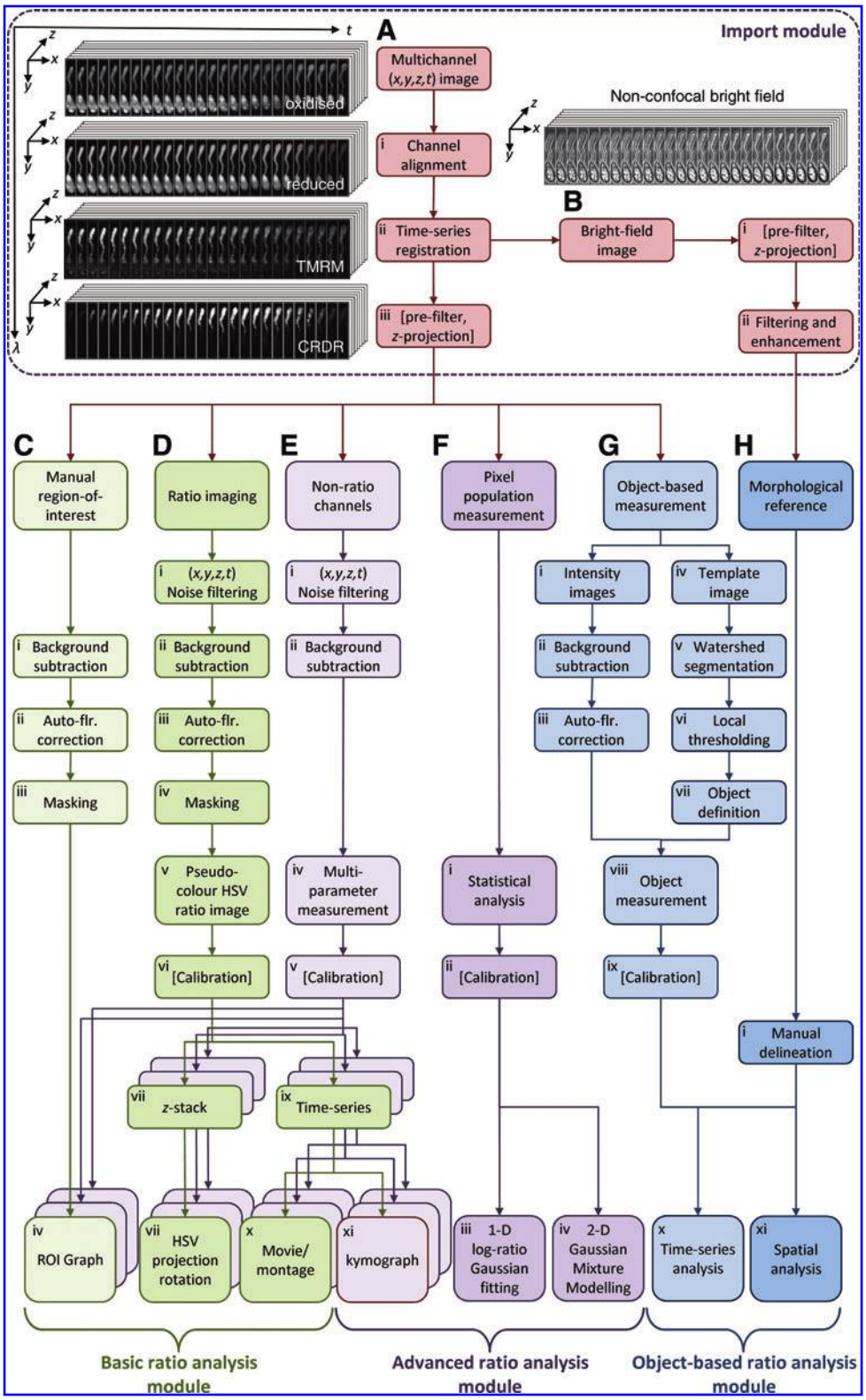

FIG. 1. Schematic diagram showing the main elements of the redox ratio analysis software. Multichannel, multi-dimensional images are loaded into the software using the import module (**(A, B)**, *red boxes*), aligned, filtered, and, if appropriate, their dimensionality is reduced using projection algorithms **(A)**. The Basic ratio analysis module (**C, D,** *green boxes*) is used to construct pseudo-color-coded ratio images **(D)**, following background subtraction and auto-fluorescence correction. Measurements are made using manually defined regions of interest **(C)**. The advanced ratio analysis module (**E, F,** *purple boxes*) extends the analysis to include multiple channels **(E)** and provides additional visualization approaches, such as kymograph plots. There are also options to analyze the whole population of pixels **(F)** using 1D fits to the log-ratio data or a 2D Gaussian mixture model (GMM) fit to the corrected intensity data. The object-based ratio analysis module (**G, H,** *blue boxes*) uses a watershed segmentation, followed by a local intensity threshold to identify individual objects. The ratio values are then calculated from the average intensity for each object. The object ratios can be analyzed as a population response **(G)** or combined with morphological information, such as cell identity or with distance from a spatial landmark, to correlate the redox behavior with the cell response **(H)**.

the statistical properties of the background can be estimated accurately and subtracted from each channel [Fig. 1D (ii)]. In addition, auto-fluorescence bleed-through into one of the measurement channels is a common problem, particularly with plant specimens and blue/violet excitation. As auto-fluorescence has structure in the image, it cannot simply be subtracted as a single value similar to background measurements. However, it is possible to estimate the auto-fluorescence from an emission wavelength range that does not have any signal from the probe. For example, with roGFP, this is possible with excitation at 405 nm and emission at 435–485 nm. As the auto-fluorescence spectrum tends to be quite

broad, a scaled version of the auto-fluorescence image can be subtracted from the probe image to correct for the auto-fluorescence bleed-through, provided the auto-fluorescence spectrum does not alter with time or treatment [Fig. 1D (iii)].

It is also useful to mask pixels with intensity values close to background or near saturation from the ratio image, or pixels that are drawn from regions with high local coefficient of variation that might correlate with edges of structures or compartments that are not well resolved, as these give a noisy and misleading impression of the real ratio value [Fig. 1D (iv)]. Without masking, edge effects from ratioing low signal intensities can be substantial and can visually dominate the ratio image in plant and fungal specimens.

For pseudo-color display [Fig. 1D (v)], the masked ratio is coded by hue on a spectral color scale ranging from blue (fully reduced) to red (fully oxidised), with the limits set by an *in situ* calibration or extrapolated from an *in vitro* calibration. The most useful initial mapping is to HSV (hue, saturation and value or intensity) color space, where the ratio is coded as hue and the average intensity from both channels gives the value. This is converted back to red, green, and blue (RGB) color space for display, and effectively gives bright colors for regions with good signals that fade to background for regions with low signals.

If the data are a time series [Fig. 1D (ix)], it can be viewed as a movie or montage. If the original data are a *z*-stack [Fig. 1D (vii)], visualization benefits from calculating rocking or tilting projections to aid 3D interpretation *via* motion parallax. Conventional rotation algorithms use maximum brightness projections of RGB images. However, this is not appropriate for color-coded ratio images. Instead, projections in HSV color space are used to record the (x,y,z) position of each voxel in maximum projection of the V channel alone. The corresponding voxel from the H and S channels is then used to reconstruct the rotated pseudo-color image [Fig. 1D (vii)].

While ratio images are a useful tool to help visualize spatial variation in signal responses, the S/N ratio is extremely low for single pixels, even after spatiotemporal smoothing. Quantitation is better achieved by manually selecting larger ROIs, which have some morphological or physiological significance (Fig. 1C). Each ROI encompasses many pixels, with corresponding improvement in S/N at the expense of spatial resolution, which can be easily presented and interpreted in graphical form [Fig. 1C (iv)].

The basic ratio program also has an option (not shown in Fig. 1), to batch process a complete set of single (x,y) images present in one folder, which is useful to compare the steady-state redox potential in multiple samples and treatments, measured over the whole image or from defined ROIs, rather than a continuous evaluation of changes in redox potential in one specimen over time.

Advanced ratio analysis

The advanced ratio program (Fig. 1E, F) extends the basic ratio analysis to handle 4D (x,y,z,t) images with a maximum of five fluorescence channels, including an auto-fluorescence channel (Fig. 1E), and parallel bright-field images (Fig. 1B). This allows correlation of changes in auto-fluorescence-corrected ratio images with a maximum of two other physiological parameters, and (non-confocal) bright-field morphology. In addition to the manual ROI measurements, movies, and montages available in the basic ratio analysis module, there is also an *x*-*t* kymograph option to represent the response along a manually defined transect as a 2D image with response on the *x*-axis and time on the *y*-axis [Fig. 1D (xi)].

Pixel-population measurements

In more complex images, such as intracellular hyphal networks during fungal infection (13), picking a few ROIs across the specimen does not provide a robust, un-biased estimate of the physiological behavior throughout the system. However, this can be achieved in the advanced module by considering the intensity or ratio information from a statistical perspective, along with estimates of the goodness of fit (Fig. 1F), and either calculating multi-component 1D Gaussian fits to the log ratio data from all pixels [Fig. 1F (iii)] or fitting 2D Gaussian mixture models (GMM) to the corrected intensity data before ratioing [Fig. 1F (iv)]. Fitting to the original intensity data or log ratio values does not take into account the relative intensity of the different pixels contributing to the distributions. Thus, ratios from very dim pixels contribute as equally as ratios from very bright pixels. A better alternative is to calculate a 1D or 2D weighted histogram in which each data point is replicated in the data set in proportion to the average intensity at each of the two wavelengths. This ensures that a large number of dim and noisy pixels do not skew the fits. The advanced ratio module includes options to explore these data fitting approaches.

Object-based ratio measurements

Transgenic reporters, such as roGFP, can be easily targeted to organelles, such as chloroplasts and mitochondria, facilitating sophisticated dissection of sub-cellular behavior. However, these organelles are present in considerable numbers (hundreds) particularly in plant and fungal cells, and are highly dynamic, making it impractical to manually select individual objects, and unhelpful to consider the total pixel population statistics described earlier, as these disguise individual organelle behavior. As an alternative, it is possible to automatically segment each organelle separately, and then calculate the average ratio values on an object-by-object basis (Fig. 1G). A wide variety of segmentation algorithms can be used, but we have found a generic two-step procedure is routinely applicable. Objects are initially separated from each other into nonoverlapping domains using watershed segmentation of an inverted template image calculated from the original intensity channels [Fig. 1G (iv–v)]. Each object definition is refined using a local intensity threshold within each watershed domain, to accommodate objects with differing overall intensity [Fig. 1G (vi)].

Once the objects are segmented, various morphological parameters can be measured automatically, along with the average intensity at each wavelength needed to calculate the ratio values. If the objects do not move during the time series, object responses can be visualized as an ''object''-time plot analogous to a kymograph [Fig. 1G (x)]. In parallel, the (non-confocal) bright-field image can be processed separately to highlight morphological features of interest, using a combination of noise filtering, projection, contrast enhancement, and manual delineation (Fig. 1B, H). Key landmarks can then be established to correlate physiological response with

cell or organelle identity, morphology, or localized event [Fig. 1G (xi)].

Calibration of the redox potential

Relative changes in ratio values can provide a reasonable amount of information for comparative studies. However, more precise calibration may be possible with experimental treatments that define the *in vivo* probe response. Ideally, each experiment should include an internal calibration at the end of the experiment by perfusion with a reductant, such as dithiothreitol (DTT), followed by an oxidant, such as H_2O_2 or aldrithiol-2(2,2′-dipyridyl disulphide) (4, 8), to drive the roGFP to a highly reduced or oxidized form, respectively. H_2O_2 has been the most widely used reagent to oxidize roGFP so far, but has the disadvantage that it is not specific for thiols and can also cause extensive formation of O_2 bubbles that perturb imaging. Aldrithiol shows greater specificity for thiols groups and avoids bubble formation. In practice, calibration values can be stored and applied to other data sets collected under identical imaging conditions. Each program has additional steps to calibrate the roGFP ratio values determined according to the following two-step process.

The degree of oxidation (*OxD*) of the roGFP sensor is calculated from Equation (1), according to (8):

$$OxD_{roGFP} = \frac{R - R_{red}}{\frac{I_{488ox}}{I_{488red}}(R_{ox} - R) + (R - R_{red})} \quad (1)$$

where R is the ratio of excitation at 405/488 nm after background subtraction and auto-fluorescence correction, R_{red} is the ratio of fully reduced form after perfusion with 10 m*M* DTT, R_{ox} is the ratio of the fully oxidized form after perfusion with 10–100 m*M* H_2O_2 or 0.1–10 m*M* aldrithiol, and I_{488ox} and I_{488red} are the intensities at 488 nm for the fully oxidized and fully reduced forms, respectively. The redox potential is then estimated from Equation (2):

$$E' = E'^{pH}_{0(roGFP)} - \frac{2.303RT}{zF}\log_{10}\frac{1 - OxD_{roGFP}}{OxD_{roGFP}} \quad (2)$$

where R is the gas constant ($8.315\,J \cdot K^{-1} \cdot mol^{-1}$), T is the absolute temperature, usually 298.15 K for plant and fungal experiments and 310.15 K for mammalian studies, z is the number of transferred electrons (2), F is the Faraday constant ($9.648 \times 10^4\ C \cdot mol^{-1}$), and $E'^{pH}_{0(roGFP)}$ is the midpoint redox potential based on the standard midpoint potential E'_0 at 30°C and pH 7, adjusted for the estimated compartment pH and experimental temperature (20–25°C) according to Equation (3):

$$E'^{pH}_{0(roGFP)} = E'_{0(roGFP)} - \frac{2.303RT}{zF}(pH - 7) \quad (3),$$

where the midpoint redox potential for roGFP1 ($E'_{0\ roGFP1}$) is −288 mV and roGFP2 ($E'_{0\ roGFP2}$) is −272 mV (8). The most useful calibration so far is the percentage oxidation, as this normalizes between different experiments and laboratories, and has an intuitive understanding, while the redox potential has additional assumptions of local compartment pH and mid-point potential.

Results

The software is applicable to many different experimental situations. Here, we describe three examples that highlight the major innovations of the approaches developed over and above the basic ratio analysis.

Application to ratio imaging of roGFP during pathogen infection

We illustrate the different modes of analysis available in the advanced ratio analysis program for multi-channel, multi-dimensional images that allow correlation between several physiological parameters measured simultaneously—in this case, quantitation of the glutathione redox potential

FIG. 2. Advanced ratio analysis: Simultaneous measurement of ROS, mitochondrial membrane potential, and glutathione redox potential in germlings of *Magnaporthe oryzae*. Germlings of *M. oryzae* **(A)** expressing cytoplasmic Grx1-roGFP2 were sequentially imaged with excitation at 405 nm **(B)** and 488 nm **(C)** as z-stacks with 2 μm spacing at 30 s time intervals, and analyzed as optimum plane projections after smoothing with a $5 \times 5 \times 3$ averaging filter and correction for bleed-through from auto-fluorescence **(D)** in the 405 nm channel. Grx1-roGFP2 was located predominantly in the cytoplasm of the basal cell (bc), mid cell (mc), and apical cell (ac), including the germ tube (gt) and appressorium (ap). Scale bar = 10 μm. Fluorescence was also observed in the vacuole, particularly in the basal and mid cells, and visible as *red* organelles in the merged image **(E)**. The degree of oxidation of the Grx1-roGFP2 was visualized from the pseudo-color-coded ratio, after calibration with 10 m*M* DTT, to reduce the internal pool and 100 m*M* H_2O_2, to oxidize it **(F)**. To quantify the responses, the average fluorescence from the appressorium was measured **(Q)**. While the cytoplasm showed a uniform low ratio **(Q)**, Grx1-roGFP2 ratios from the vacuoles indicated the probe was more oxidized, but still capable of responding to calibration **(F)**. Images are shown as every ninth image from a 132-frame sequence. ROS were mapped in parallel using CRDR (Ex. 633 nm, Em. 657–721 nm) **(G)**, while mitochondrial activity was measured using membrane-potential partitioning of TMRM (Ex. 543 nm, Em. 561–603 nm) **(H)**. Levels of ROS increased linearly in the cytoplasm of all three cells, but much more pronounced accumulation was observed in punctate structures in the appressorium **(G, J, R)**. The punctate structures labeled by CRDR overlapped with the TMRM signal **(I)**, from which we infer CRDR predominantly reported mitochondrial ROS in this system. The TMRM signal was normalized as the fold accumulation against the dye concentration in the medium **(K)**, showing a roughly 10-fold ratio **(S)** once the initial perfusion and loading had equilibrated. The roGFP signals were also plotted as a weighted 2D histogram and fit with a three-component GMM that identified three subpopulations corresponding to the cytoplasmic signals, vacuole signals, and signals during calibration with H_2O_2 **(L)**. Data were also visualized as a kymograph along a transect running along the mid-line of the germling **(M)** to capture the behavior of each cell (and sub-cellular vacuole compartments) over time for the roGFP ratio **(N)**, CRDR response **(O),** or TMRM accumulation **(P)**. CRDR, CellROX Deep Red; DTT, dithiothreitol; Grx1, human glutaredoxin 1; roGFP, reduction-oxidation-sensitive green fluorescent protein; ROS, reactive oxygen species; TMRM, tetramethyl rhodamine methyl ester.

(E_{GSH}), rates of ROS production, and mitochondrial activity in the rice blast fungus *Magnaporthe oryzae* (13). Rice blast disease caused by *M. oryzae* is a major global problem that annually causes yield losses sufficient to feed 3–10.6% of the world's population 2000 calories a day for 1 year (6). Plant defenses to pathogen attack include a rapid burst of ROS. However, ROS are also produced by normal fungal metabolism, and are known to be required for successful development of infection structures in *M. oryzae* (5, 9). It is therefore important to determine the extent to which ROS and E_{GSH} control early development in *M. oryzae* and the capacity of the glutathione anti-oxidant system to deal with an imposed oxidative burst, as might be encountered during host infection.

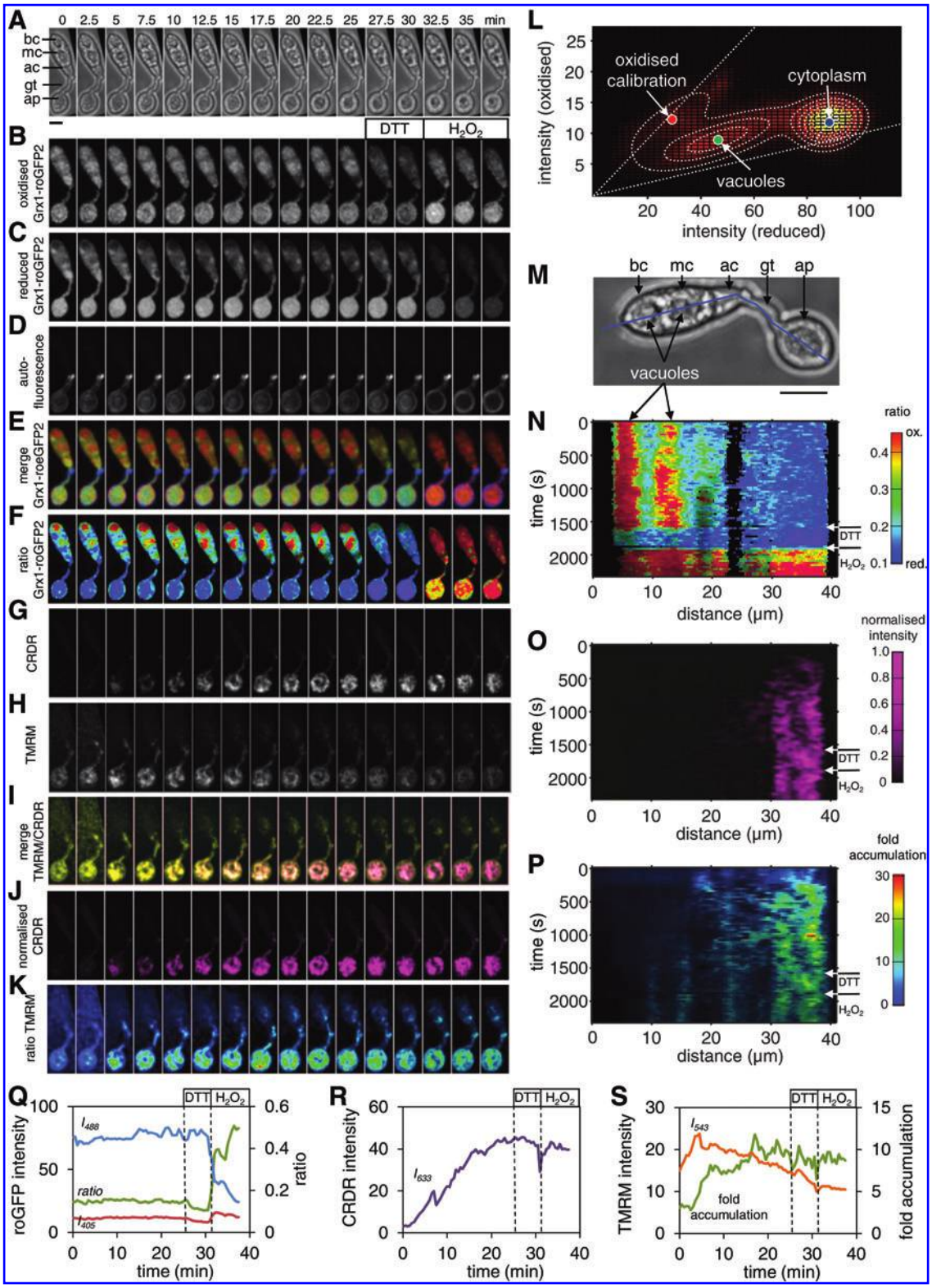

Fungal spores expressing Grx1-roGFP2 (7) showed normal rates of germ tube extension, swelling, and appressorium development (*e.g.*, Fig. 2A), and were fully pathogenic on barley and rice (data not shown). In addition to Grx1-roGFP2, ROS were labeled with CellROX Deep Red (CRDR; Life Technologies) and mitochondrial membrane potential with tetramethyl rhodamine methyl ester (TMRM; Molecular Probes). Cells were imaged using multi-channel 4D (*x,y,z,t*) with quadruple excitation and paired line switching at 405 nm and 633 nm, and 488 nm and 543 nm. Images were collected for oxidized Grx1-roGFP2 (Ex. 405 nm, Em. 500–530 nm, Fig. 2B), reduced Grx1-roGFP2 (Ex. 488 nm, Em. 500–530 nm, Fig. 2C), wall auto-fluorescence (Ex. 405 nm, Em. 435–485 nm, Fig. 2D), CRDR (Ex. 633 nm, Em. 657–721 nm. Fig. 2G), and TMRM (Ex. 543 nm, Em. 561–603 nm, Fig. 2H). A non-confocal, bright-field transmission image was collected in parallel (Fig. 2A).

The time series for *M. oryzae* was collected at 30 s intervals for 66 min in multi-track mode, as *z*-stacks of seven optical sections taken at 3 μm intervals apart, with (*x,y*) pixel sizes at 0.22 μm. Pinhole settings were adjusted individually for each channel to give an estimated optical section thickness of 2 μm. This provided some degree of optical sectioning, but with sufficient signal to noise to allow long-term physiological measurements with low laser intensities, which ranged from 1.3 to 7.3 μW at the specimen for the different wavelengths. Each 3D data stack was preprocessed by filtering with a $5 \times 5 \times 3$ averaging kernel, and the complexity reduced using the import module to extract the voxel with the highest intensity for oxidized or reduced Grx1-roGFP2 along the *z*-axis to give a single (*x,y*) image at each time point for each channel. Bright-field images were processed separately by noise filtering, MIP, and adaptive contrast-limited adaptive histogram equalization (Fig. 2A).

After the preprocessing data reduction, Grx1-roGFP2 fluorescence was observed in the cytoplasm and, to a lesser extent, vacuoles (Fig. 2B, C, E). Fluorescence with excitation at 405 nm increased with probe oxidation during calibration with H_2O_2 (Fig. 1B), while signal with 488 nm excitation decreased (Fig. 2C). However, there was also auto-fluorescence bleed-through into the Grx1-roGFP2$_{405}$ channel, typically around the site of germ tube emergence, and the appressorium wall, visible in merged images (Fig. 2D, E). To correct the Grx1-roGFP2$_{405}$ images, auto-fluorescence images were collected at 435–485 nm (Fig. 2D), scaled by an empirically determined bleed-through correction factor and subtracted. It should be noted that images in Figure 2 have been rescaled for display—the actual autofluorescence signal is typically $<5\%$ of the Grx1-roGFP2$_{405}$ signal.

Changes in Grx1-roGFP2 spectrum were visualized as pseudo-color-coded ratio images, scaled to the minimum and maximum of the *in situ* calibration values (Fig. 2F). Localization of Grx1-roGFP2 in vacuoles was not expected, but parallels other cytoplasmically expressed fluorescent proteins in *M. oryzae* germlings, such as mCherry (data not shown, see also (3), and may reflect high levels of autophagy during development in *M. oryzae* (20). Nevertheless, the Grx1-roGFP2 signal in both cytoplasmic and vacuolar compartments responded to *in situ* calibration (Fig. 2F, Q).

The ratio image indicated that all the cytoplasmic compartments in the three-celled spore, glutathione germ tube, and appressorium maintained a highly reduced redox potential (Fig. 2F). Response to calibration, measured from a manually defined ROI in the appressorium, was rapid, with reduction by DTT and oxidation by H_2O_2 complete within ~ 2 min (Fig. 2F, Q). Although H_2O_2 caused bleaching of the probe, taking the ratio corrected for the resulting changes in intensity (Fig. 2Q), giving a dynamic ratio range around four, similar to previous reports with the wavelength combinations used here (7).

It is much more difficult to measure the cytoplasm in the cells other than the appressorium with manually defined ROIs, because of the spatial overlap with vacuoles. However, a GMM fit to the entire data series clearly identified a reduced signal from the cytoplasm, a more oxidized signal from the vacuoles, and a separate signal from both the cytoplasm and vacuoles during the H_2O_2 calibration. Contour maps from the GMM were overlaid on 2D histograms generated from the weighted pixel intensities, and the intensity value of the Gaussian peak at each wavelength was used to calculate the ratio, and hence degree of oxidation and redox potential for each component (Fig. 2L). An alternative visualization approach involves constructing a kymograph along a user-defined transect (Fig. 2M) that highlights the ratio behavior of each compartment and cell type (Fig. 2N).

Simultaneously with measurements of E_{GSH}, ROS were imaged with the long-wavelength ROS probe, CRDR. The reactivity of CRDR to different ROS species has not been published, but the manufacturer reports it is more photostable, less pH sensitive, and more specific for ROS than other reactive probes. In this study, the particular benefit is that the red excitation (640 nm) and emission (665 nm) wavelengths facilitate multi-parameter imaging with roGFP and TMRM. CRDR showed a time-dependent increase in fluorescence in *M. oryzae* spores, labeling discrete punctate structures, predominantly in the appressorium (Fig. 2G, I, R, O). As CRDR is a reactive probe, the rate of ROS production is reflected in the derivative of the absolute signal. Unfortunately, this is not possible to reliably calculate from the imaging data as the punctate objects are motile, making temporal differencing irrelevant. Nevertheless, the response averaged over the entire appressorium was approximately linear over the first 20 min, suggesting a relatively constant rate of ROS production at this developmental stage (Fig. 2R).

The punctate labeling is reminiscent of mitochondrial distribution in this system, so to investigate whether the increase in CRDR fluorescence principally reflects a high level of ROS produced by mitochondrial activity (14), we tested whether the punctate CRDR structures co-localized with active mitochondria, identified by membrane potential-dependent accumulation of TMRM. TMRM labeling revealed highly motile tubular mitochondria, particularly in the appressorium (Fig. 2H), that overlapped the CRDR signal in merged images (Fig. 2G, I). As TMRM shows a Nernstian potential-sensitive accumulation in mitochondria, the fold accumulation can be estimated as a proxy for membrane potential, by ratioing against the TMRM signal in the medium (Fig. 2J, S, P). However, the absolute level of TMRM fluorescence declines through photobleaching during the experiment [the fold accumulation remains reasonably constant around 10-fold, once the initial labeling period is complete (Fig. 2S)]. Nevertheless, these fold-accumulation values underestimate the true mitochondrial potential as the volume averaging needed to achieve a reasonable S/N reduces the peak intensity attributed to individual mitochondria.

Lower levels of TMRM and CRDR accumulation were observed in the other cells throughout development, even after extended periods of probe incubation. We infer that mitochondria in these cells are in a different metabolic state, possibly geared toward synthesis of metabolic intermediates (12), rather than ATP production.

Object-based ratioing—pulsing in mitochondria

Measurement of the physiological response of individual organelles such as mitochondria is extremely time consuming if separate ROIs have to be manually applied to extract useful data. It is more convenient to automatically segment each object, and either analyze individual mitochondria that show an interesting response or determine the total population behavior. In this example, object-based measurements were used to characterize mitochondrial behavior in *Arabidopsis* epidermal cells, where individuals in the population showed transient pulses in mitochondrial membrane potential, measured using TMRM, that correlate with matrix alkalinisation, measured using circularly permutated yellow fluorescent protein (cpYFP) (15–18).

Trying to identify mitochondria that show rare pulsing behavior is quite challenging if objects have to be manually selected by the user from a field of potentially hundreds of organelles, and there is a serious risk that measurements are biased by selection of objects with the highest saliency when viewing the time series. However, fluorescently labeled objects can be readily segmented using a two-step procedure based on an initial watershed segmentation to separate objects into nonoverlapping domains, followed by a local intensity-based threshold set at the 50% value between the local maximum in each domain and the background. Using this approach, it was possible to determine the response from hundreds of mitochondria rapidly without user bias. Equally, the watershed approach can over-segment any objects with an ''hour-glass'' profiles, leading to fragmentation of long mitochondria into multiple compartments. It may be possible to develop secondary routines to ''anneal'' such fragmented objects, but these have not yet been implemented.

Typically mitochondrial behavior *in vivo* is shown in Figure 3 for a small region taken from a time series of *Arabidopsis* cells expressing mt-cpYFP and also labeled with TMRM (16). After object-based segmentation, one mitochondrion (No. 22), among the 57 present in this sub-image from more than 200 present in the entire image, showed a transient depolarization after about 10 s (loss of red TMRM signal, Fig. 3A, B) that lasted for a further 10 s and that did not occur in other mitochondria (see traces shown for two others labelled in Fig. 3A, B). Simultaneously, there was an increase in the average object cpYFP signal (Fig. 3A, C). The data were quite noisy and there were also some transient fluctuations in TMRM and cpYFP signal that did not show this inverse behavior, but reflected slight changes in position of the individual mitochondria, or indeed the whole cell (Fig. 3B, C). These fluctuations were compensated by a pseudo-ratioing approach, dividing the cpYFP signal by the TMRM signal (Fig. 3D). Alternatively, the covariance between the two signals was used to efficiently highlight the pulsing behavior as a strong transient, negative covariance.

Identifying mitochondria showing this behavior was facilitated by constructing an ''object''-time plot (Fig. 3E),

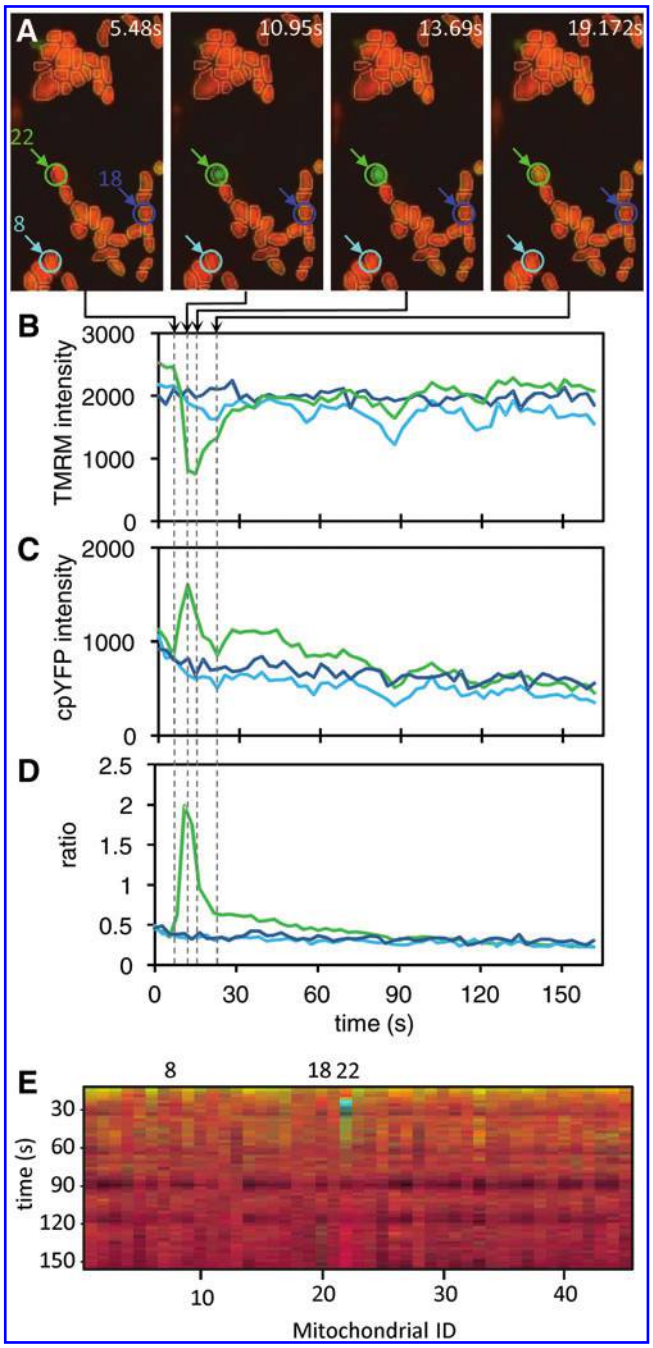

FIG. 3. Object-based ratio analysis: Measurement of pulsing in individual mitochondria. (A) Images from a time series showing a single mitochondrion from an automatically segmented population in an epidermal cell in a living *Arabidopsis* root that undergoes a transient membrane depolarization and loss of TMRM signal (*red*) concurrently with matrix alkalinisation, visible as an increase in cpYFP signal (*green*). Traces showing the TMRM signal **(B)**, cpYFP signal **(C),** and cpYFP/TMRM ratio **(D)** for the selected mitochondria highlighted in **(A)**. **(E)** An ''object'' time plot for all the mitochondria in the image with the TMRM signal (*red channel*), normalized to the median, the normalized cpYFP signal (*green*), and normalized and inverted covariance (*blue channel*). The individual pulsing mitochondrion (No. 22) is easily identified in this data presentation format. cpYFP, circularly permuted yellow fluorescent protein.

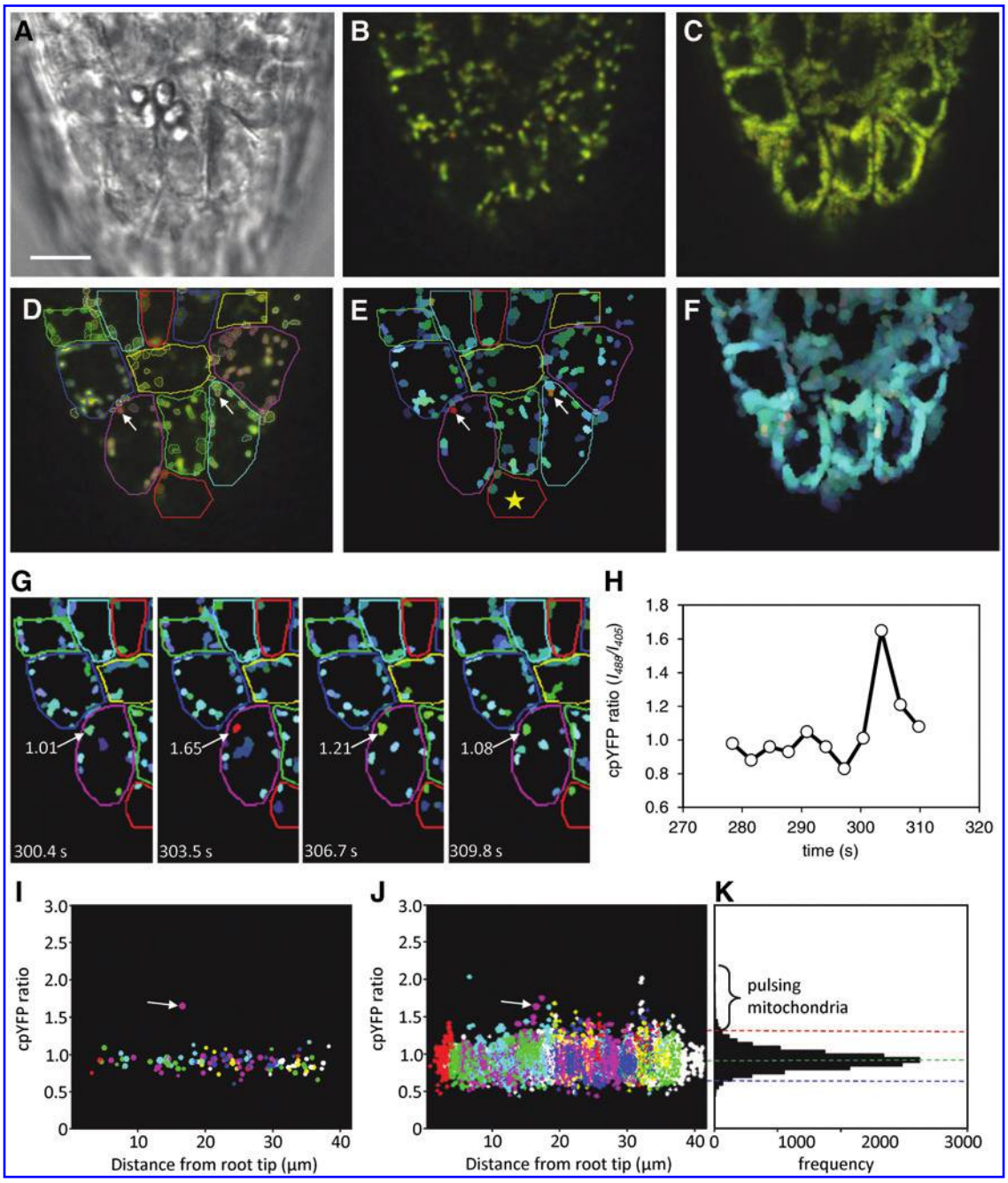

FIG. 4. Object-based ratio analysis: Measurement of mitochondrial pH pulses in *Arabidopsis* root tips. Images were collected as a time series of cpYFP fluorescence targeted to mitochondria in root cells of *Arabidopsis thaliana*. **(A)** Bright-field transmission image of the root tip, scale bar = 10 μm. **(B)** Single merged image from the time series showing cpYFP with 405 nm excitation (*red*) and 488 nm excitation (*green*). **(C)** Maximum projection over time of the cpYFP fluorescence to illustrate the circulating paths of the mitochondria around the central vacuole. **(D)** Manual delineation of the cell outlines from the bright-field image and maximum fluorescence projection. The perimeters of the segmented mitochondria are color coded to reflect the parent cell. **(E)** Pseudo-color-coded object ratio map from 0.7 (*blue*) to 1.8 (*red*). **(F)** Maximum projection over time of the object ratio values. **(G)** Time sequence showing the transient alkalinization of the mitochondrion labeled with an *arrow*. **(H)** Ratio values during the transient alkalinization. **(I)** Plot of all the object ratios with distance from the root tip (marked with an *asterisk* in **E**) at time point 303.5 s **(J)** ratio-distance plot for all objects from the complete time series. **(K)** Frequency histogram of all the ratio values. The average ratio (*green*) and the upper (*red*) and lower (*blue*) 99% confidence limits from the log ratio data are shown superimposed. Objects with ratio values greater than the upper bound were considered to be pulsing. In total, about 1% of mitochondria showed a transient alkalinization over the time period.

where the RGB image was constructed from the TMRM signal normalized to the median for each mitochondrion (red), normalized cpYFP signal (green), and inverse of the covariance (blue). The pulsing mitochondrion was clearly identifiable among the nonresponders in the object-time plot. In cells with more complex population responses, under stress treatments for example, the object responses can be sorted and classified by a relevant summary of their individual behavior, such as the maximum negative covariance in this case, which can be used both to find interesting individuals and to summarize the population response.

Object-based ratioing—correlation with morphological landmarks

In cases where the mitochondria are not stationary, it is difficult to extract ''object''-time measurements, as individual mitochondria move too fast or circulate out of the field of view or plane of focus to track reliably for more than a few frames. Nevertheless, the population behavior can still reveal interesting local phenomena. Thus, mitochondria expressing cpYFP in *Arabidopsis* root tip cells (Fig. 4A, B) are very dynamic, tending to circulate around the central vacuole to give a peripheral ring in each cell when viewed as an MIP over time (Fig. 4C). The combination of the bright-field image and projected image can be used to manually delineate each cell in the root tip (Fig. 4D).

In other systems, it might be appropriate to use additional probes to label the cell wall or the plasma membrane to achieve better cell definition, and future software releases may include an automated cell detection routine to facilitate this process. The watershed segmentation and local thresholding method identifies each mitochondrion (Fig. 4D), which can then be associated with a particular cell or compartment. The average intensity for each segmented mitochondria with 405 and 488 nm excitation was used to calculate object ratios (I_{488}/I_{405}) for the cpYFP signal from mitochondria in each cell, and used to generate a pseudocolor-coded object ratio map at each time point (Fig. 4E), or projected over the complete time sequence (Fig. 4F). The cpYFP spectrum is relatively insensitive to pH with excitation at 405 nm, while there is a substantial increase with increasing pH an excitation at 488 nm, allowing ratiometric measurements of pH. Each mitochondrion was assigned to a cell type and given a physical distance from the most distal cell in the root apex, marked with an asterisk (Fig. 4E).

While the majority of mitochondria showed low ratios between 0.7 and 1, occasionally individual mitochondria (marked with arrows (Fig. 4D, E) showed an increased ratio (color-coded red), corresponding to a more alkaline matrix. In the maximum projection over time, a number of such alkaline mitochondria are visible in different cells (Fig. 4F), but it is not clear from the single time point or the projected image whether these have constitutively higher pH, or whether these mitochondria are also showing pulsing behavior. Examination of a short time sequence shows that the behavior corresponds to a transient pulse, with the average ratio increasing from around 1 to 1.65 and back again over a 10 s window (Fig. 4G, H). An alternative approach to visualize the population response involves plotting the ratio for each mitochondrion with distance from the root tip, with the color of each point matching the parent cell (Fig. 4I). The increased ratio of one mitochondrion at time point 303.5 s is clearly visible in comparison to the population in all the other cells at this time point (Fig. 4I). Plotting data for all time points shows a number of other transient alkalinisation events in other cells (Fig. 4J) where the ratio exceeds the 99% confidence bound on the log ratio from the whole population (Fig. 4K). In total, there were 133 instances out of 13,032, where the object ratio value exceeded the upper 99% confidence limit, giving around 1% of the population pulsing at any one time (Fig. 4K).

Acknowledgments

The author is grateful to numerous colleagues for discussions over the years that have helped develop these programs, in particular Markus Schwarzlander for the images shown in Figures 2–4.

Author Disclosure Statement

No competing financial interests exist.

References

1. Aoki K, Kamioka Y, and Matsuda M. Fluorescence resonance energy transfer imaging of cell signaling from in vitro to in vivo: basis of biosensor construction, live imaging, and image processing. *Dev Growth Differ* 55: 515–522, 2013.
2. Bright GR, Fisher GW, Rogowska J, and Taylor DL. Fluorescence ratio imaging microscopy: temporal and spatial measurements of cytoplasmic pH. *J Cell Biol* 104: 1019–1033, 1987.
3. Czymmek KJ, Bourett TM, Sweigard JA, Carroll A, and Howard RJ. Utility of cytoplasmic fluorescent proteins for live-cell imaging of *Magnaporthe grisea* in planta. *Mycologia* 94: 280–289, 2002.
4. Dooley CT, Dore TM, Hanson GT, Jackson WC, Remington SJ, and Tsien RY. Imaging dynamic redox changes in mammalian cells with green fluorescent protein indicators. *J Biol Chem* 279: 22284–22293, 2004.
5. Egan MJ, Wang ZY, Jones MA, Smirnoff N, and Talbot NJ. Generation of reactive oxygen species by fungal NADPH oxidases is required for rice blast disease. *Proc Natl Acad Sci U S A* 104: 11772–11777, 2007.
6. Fisher MC, Henk DA, Briggs CJ, Brownstein JS, Madoff LC, McCraw SL, and Gurr SJ. Emerging fungal threats to animal, plant and ecosystem health. *Nature* 484: 186–194, 2012.
7. Gutscher M, Pauleau AL, Marty L, Brach T, Wabnitz GH, Samstag Y, Meyer AJ, and Dick TP. Real-time imaging of the intracellular glutathione redox potential. *Nat Methods* 5: 553–559, 2008.
8. Hanson GT, Aggeler R, Oglesbee D, Cannon M, Capaldi RA, Tsien RY, and Remington SJ. Investigating mitochondrial redox potential with redox-sensitive green fluorescent protein indicators. *J Biol Chem* 279: 13044–13053, 2004.
9. Heller J and Tudzynski P. Reactive oxygen species in phytopathogenic fungi: signaling, development, and disease. *Annu Rev Phytopathol* 49: 369–390, 2011.
10. Miyawaki A. Development of probes for cellular functions using fluorescent proteins and fluorescence resonance energy transfer. *Annu Rev Biochem* 80: 357–373, 2011.
11. Okumoto S, Jones A, and Frommer WB. Quantitative imaging with fluorescent biosensors. *Annu Rev Plant Biol* 63: 663–706, 2012.

12. Patkar RN, Ramos-Pamplona M, Gupta AP, Fan Y, and Naqvi NI. Mitochondrial beta-oxidation regulates organellar integrity and is necessary for conidial germination and invasive growth in *Magnaporthe oryzae*. *Mol Microbiol* 86: 1345–1363, 2012.
13. Samalova M, Meyer AJ, Gurr SJ, and Fricker MD. Robust anti-oxidant defences in the rice blast fungus *Magnaporthe oryzae* confer tolerance to the host oxidative burst. *New Phytol* 201: 556–573, 2014.
14. Schwarzlander M and Finkemeier I. Mitochondrial energy and redox signaling in plants. *Antioxid Redox Signal* 18: 2122–2144, 2013.
15. Schwarzlander M, Logan DC, Fricker MD, and Sweetlove LJ. The circularly permuted yellow fluorescent protein cpYFP that has been used as a superoxide probe is highly responsive to pH but not superoxide in mitochondria: implications for the existence of superoxide 'flashes'. *Biochem J* 437: 381–387, 2011.
16. Schwarzlander M, Logan DC, Johnston IG, Jones NS, Meyer AJ, Fricker MD, and Sweetlove LJ. Pulsing of membrane potential in individual mitochondria: a stress-induced mechanism to regulate respiratory bioenergetics in *Arabidopsis*. *Plant Cell* 24: 1188–1201, 2012.
17. Schwarzlander M, Murphy MP, Duchen MR, Logan DC, Fricker MD, Halestrap AP, Muller FL, Rizzuto R, Dick TP, Meyer AJ, and Sweetlove LJ. Mitochondrial 'flashes': a radical concept repHined. *Trends Cell Biol* 22: 503–508, 2012.
18. Schwarzlander M, Wagner S, Ermakova YG, Belousov VV, Radi R, Beckman JS, Buettner GR, Demaurex N, Duchen MR, Forman HJ, Fricker MD, Gems D, Halestrap AP, Halliwell B, Jakob U, Johnston IG, Jones NS, Logan DC, Morgan B, Muller FL, Nicholls DG, Remington SJ, Schumacker PT, Winterbourn CC, Sweetlove LJ, Meyer AJ, Dick TP, and Murphy MP. The 'mitoflash' probe cpYFP does not respond to superoxide. *Nature* 514: E12–E14, 2014.
19. Stein F, Kress M, Reither S, Piljic A, and Schultz C. FluoQ: a tool for rapid analysis of multiparameter fluorescence imaging data applied to oscillatory events. *ACS Chem Biol* 8: 1862–1868, 2013.
20. Talbot NJ, Kershaw MJ, and Saunders DOC. Investigating infection-associated autophagy in the rice blast fungus *Magnaporthe oryzae*. *Autophagy* 5: 903–903, 2009.
21. Tanasugarn L, McNeil P, Reynolds GT, and Taylor DL. Microspectrofluorometry by digital image-processing: measurement of cytoplasmic pH. *J Cell Biol* 98: 717–724, 1984.
22. Tsien RY. Nobel lecture: constructing and exploiting the fluorescent protein paintbox. *Integr Biol (Camb)* 2: 77–93, 2010.

Address correspondence to:
Prof. Mark D. Fricker
Department of Plant Sciences
University of Oxford
South Parks Road
Oxford OX1 3RB
United Kingdom

E-mail: mark.fricker@plants.ox.ac.uk

Date of first submission to ARS Central, May 21, 2015; date of acceptance, May 27, 2015.

Abbreviations Used

cpYFP = circularly-permuted yellow fluorescent protein
CRDR = CellROX Deep Red
DTT = dithiothreitol
E_{GSH} = glutathione redox potential
GMM = Gaussian mixture model
Grx1 = human glutaredoxin 1
HSV = hue, saturation, value color space
MIP = maximum intensity projection
OxD = degree of oxidation
RGB = red, green, blue
roGFP = reduction-oxidation-sensitive green fluorescent protein
ROI = region of interest
ROS = reactive oxygen species
S/N = signal-to-noise ratio
TMRM = tetramethyl rhodamine methyl ester